Supplementary Information for

Discrete symmetries control geometric mechanics in parallelogram-based origami

James McInerney, Glaucio H. Paulino and D. Zeb Rocklin

Corresponding Author James McInerney or D. Zeb Rocklin.
E-mail: jmcinern@umich.edu or zebrocklin@gatech.edu

This PDF file includes:

Figs. S1 to S3
Tables S1 to S2
Legends for Movies S1 to S4
SI References

Other supplementary materials for this manuscript include the following:

Movies S1 to S4

1. Rigidly foldable ground states of four-parallelogram origami

Here, we provide additional details about the four-parallelogram origami family of crease patterns. First, we discuss subsets and the limiting cases of previously studied patterns. Then, we parameterize the degenerate ground states of generic four-parallelogram origami. For completeness, we discuss this parameterization in regards to branching from the flattened state of developable crease patterns.

A. Four-parallelogram origami and limiting cases. Four-parallelogram origami geometries can be specified by four sector angles and four edge lengths, both defined in the vicinity of a single vertex as shown in S1A. Since each face is a parallelogram, the adjacent sector angles are supplementary, $\pi - \alpha$ and the non-adjacent angles are identical. Furthermore, since there are only four parallelogram faces, the four edge lengths determine all eight of the edges in the unit cell. Hence, generic members correspond to a point in the eight-dimensional space of geometries where one such dimension simply rescales the entire sheet.

This eight-dimensional space of geometries contains multiple subspaces of interest. First, developable crease patterns have the one-dimensional constraint on their four sector angles:

$$\alpha_A + \alpha_B + \alpha_C + \alpha_D = 2\pi, \tag{1}$$

which is a seven-dimensional subspace. Similarly, orthotropic crease patterns have a four-dimensional constraint that couples their sector angles and edge directions:

$$\boldsymbol{\ell}_1 \cdot \boldsymbol{\ell}_2 = (\mathbf{r}_1 + \mathbf{r}_3) \cdot (\mathbf{r}_2 + \mathbf{r}_4) = r_1 r_2 \cos\alpha_A - r_2 r_3 \cos\alpha_B + r_3 r_4 \cos\alpha_C - r_1 r_4 \cos\alpha_D = 0,, \tag{2}$$

which again is a seven-dimensional subspace. The Miura-ori belongs to the special case of developable, orthotropic crease patterns satisfying $\alpha_A = \alpha_B$, $\alpha_C = \alpha_D = \pi - \alpha_A$ (1, 2). The eggbox belongs to the special case of orthotropic crease patterns satisfying $\alpha_A = \alpha_B = \alpha_C = \alpha_D$ (3). Both of these crease patterns are special cases of the orthotropic Morph which itself satisfies $\alpha_A = \alpha_B$, $\alpha_C = \alpha_D$ (4).

B. Degenerate ground states. The ground states of these crease patterns are parameterized by the four dihedral angles defined in the vicinity of a vertex as shown in Fig. S1A. Since the crease pattern is spatially periodic, the remaining dihedral angles must be the complement of their parallel counterparts, $2\pi - \gamma$. Hence, the unit cell can be rigidly folded provided that the changes to these four dihedral angles are compatible with the four sector angles. Such configurations can be provided by applying spherical trigonometry to the projection of the four-coordinated vertex onto the unit sphere as shown in Fig. S1B.

The configurations of such a spherical quadrilateral are determined by triangulating the quadrilateral with a single great circle and enforcing compatibility between the two resulting spherical triangles shown in Fig. S1B. These triangles obey the spherical trigonometric relations:

$$\begin{aligned}
\cos\alpha_{24} = \cos\alpha_A \cos\alpha_D + \sin\alpha_A \sin\alpha_D \cos\gamma_1 &= \cos\alpha_B \cos\alpha_C + \sin\alpha_B \sin\alpha_C \cos\gamma_3, \\
\cos\sigma_1 = \frac{\cos\alpha_D - \cos\alpha_{24}\cos\alpha_A}{\sin\alpha_{24}\sin\alpha_A}, &\qquad \cos\sigma_4 = \frac{\cos\alpha_A - \cos\alpha_{24}\cos\alpha_D}{\sin\alpha_{24}\sin\alpha_D}, \\
\cos\sigma_2 = \frac{\cos\alpha_C - \cos\alpha_{24}\cos\alpha_B}{\sin\alpha_{24}\sin\alpha_C}, &\qquad \cos\sigma_3 = \frac{\cos\alpha_B - \cos\alpha_{24}\cos\alpha_C}{\sin\alpha_{24}\sin\alpha_B},
\end{aligned} \tag{3}$$

$$\frac{\sin\gamma_1}{\sin\alpha_{24}} = \frac{\sin\sigma_1}{\sin\alpha_D} = \frac{\sin\sigma_4}{\sin\alpha_A}, \qquad \frac{\sin\gamma_3}{\sin\alpha_{24}} = \frac{\sin\sigma_2}{\sin\alpha_C} = \frac{\sin\sigma_3}{\sin\alpha_B}. \tag{4}$$

These formulae give γ_3 in terms of γ_1 or vice versa noting there are always two solutions because arccos is multivalued over the unit circle. Once this is chosen, the diagonal α_{24} can be determined to compute the remaining interior angles σ_i and sum them for the last two dihedral angles γ_2, γ_4. Importantly, the arctan function ensures that the branches are appropriately determined:

$$\gamma_2 = \arctan\frac{\sin\gamma_1 \sin\alpha_D \sin\alpha_A}{\cos\alpha_D - \cos\alpha_{24}\cos\alpha_A} + \arctan\frac{\sin\gamma_1 \sin\alpha_A \sin\alpha_D}{\cos\alpha_A - \cos\alpha_{24}\cos\alpha_D} \tag{5}$$

$$\gamma_4 = \arctan\frac{\sin\gamma_3 \sin\alpha_C \sin\alpha_B}{\cos\alpha_C - \cos\alpha_{24}\cos\alpha_B} + \arctan\frac{\sin\gamma_3 \sin\alpha_B \sin\alpha_C}{\cos\alpha_B - \cos\alpha_{24}\cos\alpha_C}. \tag{6}$$

Once these dihedral angles are determined at a single vertex, it is easy to see the compatibility of adjacent vertices in four-parallelogram origami by substitution of the appropriate sector angles: when the dihedral angles are fixed to be identical on an edge shared by two vertices, the supplementary condition on the sector angles ensures that the edges which are not shared have complementary dihedral angles.

In principle, the choice to complete this parameterization by varying γ_1 or γ_3 is trivial; however, their domains are generically distinct because the domain of arccos used to compute the diagonal restricts the admissible dihedral angles. For example:

$$\gamma_1 = 0 \implies \alpha_{24} = \arccos\Big(\cos\alpha_A \cos\alpha_D + \sin\alpha_A \sin\alpha_D\Big), \tag{7}$$

$$\gamma_1 = \pi \implies \alpha_{24} = \arccos\Big(\cos\alpha_A \cos\alpha_D - \sin\alpha_A \sin\alpha_D\Big), \tag{8}$$

which must hold for γ_3 replacing $\alpha_A \to \alpha_B$ and $\alpha_D \to \alpha_C$ though α_{24} is only real-valued provided the arguments are over the interval $[0,1]$ implying one edge may open or close while the other may be locked from doing so. Accordingly, the diagonal is bounded:

$$\alpha_{24}^{\min} = \max\Big(|\alpha_A - \alpha_D|, |\alpha_B - \alpha_C|\Big), \qquad \alpha_{24}^{\max} = \min\Big(|\alpha_A + \alpha_D|, |\alpha_B + \alpha_C|\Big), \tag{9}$$

where the inner product $|x| = \min(x, 2\pi - x)$ is the geodesic length of the corresponding great circle taking x to always be positive valued. Hence, there are two distinct cases: the same sector angle pair determines both bounds or each sector angle pair determines a single bound. In the former, the corresponding dihedral angle's domain contains both the opened state π and the closed state 0 (and hence also 2π implying the configuration space is a non-contractible loop. In the latter, the corresponding dihedral angle's domain contains only contains 0 or π so that these two solutions join to form a single contractible loop in the configuration space. In special cases, both pairs simultaneously bound the diagonal so that the vertex is flat-foldable (in the generalized sense that two of the four dihedral angles may still be π) or developable.

C. Folding near the flattened state. Generically, the diagonal satisfies

$$\cos\alpha_{24} = \cos\alpha_A \cos\alpha_D + \sin\alpha_A \sin\alpha_D \cos\gamma_1, \tag{10}$$

which, in the flattened state of a developable crease pattern, $\gamma_1 = 0$, take on the value:

$$\alpha_{24}^{f} = \min\Big(\alpha_A + \alpha_D, 2\pi - (\alpha_A + \alpha_D)\Big). \tag{11}$$

Moreover the developability condition $\sum_i \alpha_{A_i} = 2\pi$ indicates that the dividing great circle lies either along $\alpha_A + \alpha_D$ or $\alpha_B + \alpha_C$. This means if σ_1, σ_2 are the two interior angles obtained by the great circle α_{24}^f dividing γ_2 then the $\gamma_2 = \sigma_1$ or σ_2 where the alternate interior angle is zero. Suppose that this is σ_1 so that $\alpha_{24}^f = \alpha_B + \alpha_C$ where the following holds for σ_2 under the substitution $\gamma_1 \to \gamma_3$, $\alpha_A \to \alpha_B$, and $\alpha_D \to \alpha_C$. Then by the spherical law of sines and cosines:

$$\frac{\sin\sigma_1}{\sin\alpha_D} = \frac{\sin\gamma_1}{\sin\alpha_{24}^f}, \qquad \cos\alpha_D = \cos\alpha_A \cos\alpha_{24}^f - \sin\alpha_A \sin\alpha_{24}^f \cos\sigma_1, \qquad \tan\sigma_1 = \frac{\sin\gamma_1 \sin\alpha_A \sin\alpha_D}{\cos\alpha_B - \cos\alpha_A \cos\alpha_{24}^f}. \tag{12}$$

On the other hand, α_{24}^f divides when the law of cosines satisfies:

$$\cos\alpha_{24}^f = \cos\alpha_B \cos\alpha_C + \sin\alpha_B \sin\alpha_C \cos\gamma_3. \tag{13}$$

Thus, expanding about $\sigma_1 = \pi$ and $\gamma_1 = \pi$ yields the linearly compatible differentials

$$\begin{aligned} d\gamma_2 &= -\frac{d\gamma_1 \sin\alpha_A \sin\alpha_D}{\cos\alpha_D - \cos\alpha_A \cos\alpha_{24}^f}, \qquad d\gamma_4 = -\frac{d\gamma_1 \sin\alpha_A \sin\alpha_D}{\cos\alpha_A - \cos\alpha_D \cos\alpha_{24}^f}, \\ d\gamma_3 &= \pm\left(\frac{\sin\alpha_A \sin\alpha_D (d\gamma_1)^2 + \cos\alpha_B \cos\alpha_C - \cos\alpha_A \cos\alpha_D}{\sin\alpha_B \sin\alpha_C}\right)^{\frac{1}{2}}, \end{aligned} \tag{14}$$

which determine the linear planar modes that generate the two branches intersecting at the flattened state.

2. Compatibility conditions in four-parallelogram origami

Here, we explicitly derive the linear compatibility conditions and their solutions for four-parallelogram origami. We also compute the non-trivial face amplitudes for the antisymmetric bend mode and discuss normalization of the linear isometries.

A. Four-parallelogram compatibility matrix. The main text characterizes linear isometries via compatibility constraints on vertex amplitudes and face amplitudes. Here, we discuss the physical meaning of these amplitudes and explicitly write the compatibility matrix for generic four-parallelogram origami sheets.

First, consider a crease pattern composed of rigid quadrilateral faces that is only allowed to fold along its predefined creases, and assume that each vertex is four coordinated. For a single vertex, changes in the dihedral angle of each crease, ϕ_i, generate infinitesimal rotations of the adjoined panels that are constrained by the compatibility condition

$$\sum_i \phi_i \hat{v}_i = 0, \tag{15}$$

so that these rotations vanish over a closed loop around the vertex. As discussed in the main text, this constraint admits local solutions of the form $\phi_i = (-1)^i \mathcal{V} \hat{v}_{i+1} \cdot \hat{v}_{i+2} \times \hat{v}_{i+3}$ where $\mathcal{V}$ is the *vertex amplitude* that determines the *magnitude* of the folding along each of these creases and the edge index increases cyclically in counter-clockwise order around the vertex.

This vertex amplitude is trivial when considering a single vertex, but specifies the relative amount of each folding mode when considering multiple crease-sharing vertices. For example, suppose two vertices, denoted by a and b, share an edge, denoted by i. Then a folding motion that is uniform along the crease, $\phi_i^a = \phi_i^b$, requires that $\mathcal{V}^a \hat{v}_{i+1}^a \cdot \hat{v}_{i+2}^a \times \hat{v}_{i+3}^a = \mathcal{V}^b \hat{v}_{i+1}^b \cdot \hat{v}_{i+2}^b \times \hat{v}_{i+3}^b$

where only the direction of the shared edge is necessarily equal, $\hat{v}_i^a = \hat{v}_i^b$. Thus, these two vertices fold compatibly when $\mathcal{V}^b = \mathcal{V}^a \left(\hat{v}_{i+1}^a \cdot \hat{v}_{i+2}^a \times \hat{v}_{i+3}^a\right) / \left(\hat{v}_{i+1}^b \cdot \hat{v}_{i+2}^b \times \hat{v}_{i+3}^b\right)$. This extends to closure conditions on the geometry of vertices enclosing quadrilateral face similar to the "marching algorithms" developed in Refs. (5, 6).

Second, consider an isolated quadrilateral face that is allowed to undergo low-energy bending deformations, provided that the face does not stretch. This bending can be described by a scalar on each edge, called the torsion τ_i, that determines the amount of rotation the bending induces on the local normal vector. Importantly, this bending induces displacements of the vertices of the faces so that the requirements for an isometry of the face are:

$$\sum_i \tau_i \hat{v}_i = 0, \quad \tau_1 \hat{v}_1 \times \mathbf{v}_2 = \tau_4 \hat{v}_4 \times \mathbf{v}_3, \tag{16}$$

where the edge vectors point counterclockwise around the face. For parallelogram faces in particular, these constraints exhibit solutions of the form $\tau_i = (-1)^i \mathcal{F} v_i$ where $\mathcal{F}$ is the *face amplitude* that determines the *magnitude* of the bending of the face.

Similar to the amplitude of the four-coordinated vertex discussed above, this face amplitude is entirely trivial for a single face but specifies the relative amount of each bending mode when considering multiple crease-sharing faces. For example, suppose two faces, denoted by A and B, share an edge, denoted by i. Then a bending motion that is uniform along the crease, $\tau_i^A = \tau_i^B$, requires that $\mathcal{F}^A = \mathcal{F}^B$ because the geometric factors are always identical. This remarkable result implies that origami sheets composed of *any* number of parallelogram faces always exhibits a mode that consists entirely of face bending, which we have not seen presented in the existing literature.

The two examples above elucidate the physical significance of the vertex and face amplitudes in pure-folding and pure-bending modes, respectively; however, the strength of this formalism is best exemplified by considering modes that couple folding and bending and hence, couple the vertex and face amplitudes to one another. Traditionally, such modes are described by triangulating the quadrilateral faces so that each vertex is six coordinated and imposing the vertex compatibility condition in Eqn. (15), which no longer admits analytical solutions for arbitrary geometries.

Instead, we consider compatibility along generic loops over the origami and acknowledge that such loops may be decomposed into loops around individual vertices, faces, and edges. The above analysis provides solutions to vertex and face compatibility in terms of the vertex and face amplitudes, while edge compatibility, which specifies the amount of rotation induced by a frame *across* the edge at each vertex that it touches and *along* the edge on each face that it touches, couples the vertex and face amplitudes to one another.

Interestingly, we found that for origami sheets composed of parallelogram faces, the face amplitudes can be eliminated from these constraints via appropriate linear combinations of the edge compatibility conditions, thereby yielding mathematically convenient, self-adjoint (Hermitian) operator with the property that its nontrivial nullspace describes the vertex amplitudes consistent with an isometry. These same linear combinations of edge constraints can then be used to determine the face amplitudes from the vertex amplitudes of a linear isometry and accordingly, determine the rotations and displacements of elements of the origami sheet. Thus, the vertex and face amplitudes serve as mathematical tools that represent the relative amount of *local* isometries (folding and bending, respectively) that combines to yield a *global* isometry.

The linear isometries of any parallelogram-based origami sheet are spanned by the vertex amplitudes satisfying the vertex compatibility condition

$$\sum_{i'} \left(\frac{\zeta_{i'}^a}{v_{i'}^a} \mathcal{V}^a - \frac{\zeta_{i'+2}^{a'}}{v_{i'+2}^{a'}} \mathcal{V}^{a'} \right) = 0, \tag{17}$$

in addition to the uniform face-bending mode where $\mathcal{F} = 1$ on every face. In four-parallelogram origami, these *local* coefficients are proportional to the *global* coefficients:

$$\chi_i \equiv \frac{\mathbf{r}_{i+2} \cdot \mathbf{r}_{i+3} \times \mathbf{r}_{i+4}}{R} = \frac{\hat{r}_{i+2} \cdot \hat{r}_{i+3} \times \hat{r}_{i+4}}{r_i}, \quad R \equiv r_1 r_2 r_3 r_4, \tag{18}$$

as shown in Table S2. Denoting the sums and differences $\chi_{ij}^{\pm} = \chi_i \pm \chi_j$, the corresponding compatibility matrix is:

$$\mathbf{C} = \begin{pmatrix} \chi_{13}^- + \chi_{24}^- & -\chi_{13}^- & 0 & -\chi_{24}^- \\ -\chi_{13}^- & \chi_{13}^- - \chi_{24}^- & \chi_{24}^- & 0 \\ 0 & \chi_{24}^- & -\chi_{13}^- - \chi_{24}^- & \chi_{13}^- \\ -\chi_{24}^- & 0 & \chi_{13}^- & -\chi_{13}^- + \chi_{24}^+ \end{pmatrix}. \tag{19}$$

Since the compatibility matrix anticommutes with the permutation operator, $\mathcal{P}_d \mathbf{C} \mathcal{P}_d = -\mathbf{C}$, it is off-block diagonal in the eigenbasis of this operator:

$$\mathbf{C}^{\mathrm{sym}} = \mathbf{S}^{-1}\mathbf{C}\mathbf{S} = \begin{pmatrix} 0 & 0 & 0 & 0 \\ 0 & 0 & \chi_{24}^{-} & \chi_{13}^{-} \\ 0 & \chi_{24}^{-} & 0 & 0 \\ 0 & \chi_{13}^{-} & 0 & 0 \end{pmatrix}, \quad \mathbf{S} = \frac{1}{2}\begin{pmatrix} 1 & 1 & 1 & 1 \\ 1 & -1 & 1 & -1 \\ 1 & 1 & -1 & -1 \\ 1 & -1 & -1 & 1 \end{pmatrix}, \quad \mathcal{P}_d = \begin{pmatrix} 0 & 0 & 1 & 0 \\ 0 & 0 & 0 & 1 \\ 1 & 0 & 0 & 0 \\ 0 & 1 & 0 & 0 \end{pmatrix},$$
$$|{+}{+}\rangle = \frac{1}{2}\begin{pmatrix} +1 \\ +1 \\ +1 \\ +1 \end{pmatrix}, \quad |{-}{-}\rangle = \frac{1}{2}\begin{pmatrix} +1 \\ -1 \\ +1 \\ -1 \end{pmatrix}, \quad |{+}{-}\rangle = \frac{1}{2}\begin{pmatrix} +1 \\ +1 \\ -1 \\ -1 \end{pmatrix}, \quad |{-}{+}\rangle = \frac{1}{2}\begin{pmatrix} +1 \\ -1 \\ -1 \\ +1 \end{pmatrix}. \tag{20}$$

B. Mapping from vertex to face amplitudes. The vertex amplitudes, $|\mathcal{V}\rangle$, that correspond to linear isometries, $\mathbf{C}\,|\mathcal{V}\rangle = \mathbf{0}$, generically induce some bending of the faces as indicated by edge compatibility for arbitrary parallelogram-based origami sheets:

$$\mathcal{F}^{A'} - \mathcal{F}^{A} = \mathcal{V}^{a'}\frac{\zeta_{i+2}^{a'}}{v_{i+2}^{a'}} - \mathcal{V}^{a}\frac{\zeta_i^a}{v_i^a}. \tag{21}$$

Thus, the *difference* between the amplitude on a generic face and some reference face can be recursively determined by constructing a path between them. For consistency, such face amplitudes should be orthogonal to the uniform face-bending mode. For four-parallelogram origami, this procedure yields the following orthogonal basis for the linear isometries:

$$|\mathcal{V}_+\rangle = |{+}{+}\rangle\,, \quad |\mathcal{F}_+\rangle = \mathbf{0}, \tag{22}$$
$$|\mathcal{V}_-\rangle = \mathcal{N}_-\Big(\chi_{13}^{-}\,|{+}{-}\rangle - \chi_{24}^{-}\,|{-}{+}\rangle\Big), \quad |\mathcal{F}_-\rangle = \frac{\mathcal{N}_-}{2}\Big(\chi_{13}^{+}\chi_{24}^{-}\,|{+}{-}\rangle + \chi_{13}^{-}\chi_{24}^{+}\,|{-}{+}\rangle + \chi_{13}^{-}\chi_{24}^{-}\,|{-}{-}\rangle\Big), \tag{23}$$
$$|\mathcal{V}_0\rangle = \mathbf{0}, \quad |\mathcal{F}_0\rangle = \mathcal{N}_0\,|{+}{+}\rangle\,, \tag{24}$$

where the coefficients, $\mathcal{N}$, are normalization factors. Note that these factors cannot simultaneously impose normalization of the vertices and face but instead can be chosen to satisfy $\langle\mathcal{V}|\mathcal{V}\rangle + \langle\mathcal{F}|\mathcal{F}\rangle = 1$.

C. Mapping from amplitudes to dihedral angle changes. The description of the linear isometries of origami sheets in terms of the vertex and face amplitudes is equivalent to the common formalism in which face bending is represented in terms of bending along a virtual diagonal. This equivalence fixes the orientations of the edges and the positions of the vertices, but not the orientations of the faces, since the different schemes use different definitions for how the orientation varies along a face. Here, we discuss the mapping between these two formalisms.

First, consider the parallelogram face shown in Fig. S2 which triangulated by introducing the virtual crease. In the amplitude formalism, there is an angular velocity gradient between the bottom left, (a, A), and top right, (a', A), corners of the face: $\boldsymbol{\omega}^{(a',A)} - \boldsymbol{\omega}^{(a,A)} = \tau_1^A\hat{r}_1 + \tau_2^A\hat{r}_2 = -\mathcal{F}^A(\mathbf{r}_1 - \mathbf{r}_2)$. In the dihedral angle formalism, there is an angular velocity gradient between the two triangular sections divided by the virtual crease: $\delta_1\frac{\mathbf{r}_2-\mathbf{r}_1}{|\mathbf{r}_2-\mathbf{r}_1|}$. The requirement that these two formalisms are equivalent enforces the relationship: $\delta_1 = |\mathbf{r}_2 - \mathbf{r}_1|\mathcal{F}^A$. Considering the triangulation of the generic four-parallelogram origami crease pattern shown in Fig. S2, the uniform face mode predicted by the amplitude formalism matches up with the mode with folding localized on the virtual creases.

Next, consider the adjacent parallelogram faces shown in Fig. S2. In the amplitude formalism, there is an angular velocity gradient between the bottom right corner of the first face, (a'', A), and the top left corner of the right face, (a', A'), which is equal to: $\boldsymbol{\omega}^{(a',A')} - \boldsymbol{\omega}^{(a'',A)} = \tau_2^{A'}\hat{r}_2 - \phi_2^{a'}\hat{r}_2 = \mathcal{F}^A\mathbf{r}_2 - \chi_2\mathcal{V}^{a'}\mathbf{r}_2$. In the dihedral angle formalism, there is an angular velocity gradient between the triangular sections of the left and right sides of the crease that is equal to: $\phi_2\hat{r}_2$. The requirement that these two formalisms are equivalent enforces the relationship: $\phi_2 = (\mathcal{F}^A - \chi_2\mathcal{V}^A)r_2$. The symmetric mode predicted by the amplitude formalism matches up with the mode with folding localized on the real creases. However, this is not the case for the antismymetric mode predicted by the amplitude formalism which includes an additional term proportional to the face bending. We have two options for computing this (cross the edge and then travel along it, or go in the opposite order) but the edge compatibility condition is exactly the requirement that these give the same result. Thus, the nonuniform face orientations lead to different definitions in fold angles between the different formalisms for generic modes.

3. Lattice strain and curvature

Here, we explicitly derive the local stretches of the lattice vectors due to linear isometries and relate them to the intercellular rotations of the origami sheet.

The changes in the lattice vectors measured from a corner in the vicinity of a particular vertex are obtained by the double integration between this vertex is adjacent cells:

$$\boldsymbol{\Delta}_1^{(a,A)} = \left(\tau_1^A \hat{v}_1^a - \phi_2^{\mathcal{P}_h a} \hat{v}_2^{\mathcal{P}_h a}\right) \times \mathbf{v}_1^{\mathcal{P}_h a} + \mathbf{f}_1(A) \times \boldsymbol{\ell}_1, \quad [25]$$
$$\boldsymbol{\Delta}_2^{(a,A)} = \left(\tau_4^A \hat{v}_2^a + \phi_1^{\mathcal{P}_v a} \hat{v}_1^{\mathcal{P}_v a}\right) \times \mathbf{v}_2^{\mathcal{P}_v a} + \mathbf{f}_2(A) \times \boldsymbol{\ell}_2. \quad [26]$$

Here, the vertex folds, ϕ_i^a, and face torsions, τ_i^A, satisfy the compatibility conditions for linear isometries and $\mathbf{f}(A)$ accounts for any additional vertex folding due to the face that the corner is on as indicated by the solid gray paths in Fig. S3A. Note that such face-dependent vertex folding is always on either edge $i = 2$ or $i = 4$ for $\boldsymbol{\Delta}_1$ and either edge $i = 1$ or $i = 3$ for $\boldsymbol{\Delta}_2$. Furthermore, the lattice vectors can be written in terms of the local edge vectors as $\boldsymbol{\ell}_1 = \mathbf{v}_1^a - \mathbf{v}_3^a$ and $\boldsymbol{\ell}_2 = \mathbf{v}_2^a - \mathbf{v}_4^a$, and take this same form under any permutation.

A. Lattice vector stretches. First, consider their stretches computed by projection onto the same lattice vectors. Clearly, the face-dependent terms, $\mathbf{f}(A)$ vanish since their displacements are orthogonal to the lattice vector. Since the triple product coefficients of the torsions contain redundant edge vectors in both cases, these stretches are independent of face amplitude. In contrast, the triple product coefficients of the folds contain one nonredundant term that yields the vertex folding coefficients

$$\boldsymbol{\Delta}_1^a \cdot \boldsymbol{\ell}_1 = -\mathcal{V}^{\mathcal{P}_h a} v_1^{\mathcal{P}_h a} v_3^{\mathcal{P}_h a} \zeta_2^{\mathcal{P}_h a} \zeta_4^{\mathcal{P}_h a}, \quad [27]$$
$$\boldsymbol{\Delta}_2^a \cdot \boldsymbol{\ell}_2 = \mathcal{V}^{\mathcal{P}_v a} v_2^{\mathcal{P}_v a} v_4^{\mathcal{P}_v a} \zeta_1^{\mathcal{P}_v a} \zeta_3^{\mathcal{P}_v a}, \quad [28]$$

where the face dependence has been dropped because it is always negligible. Since these pairings of vertex folding coefficients are invariant under all permutations, the lattice vector stretches depend locally only on the vertex amplitude:

$$\boldsymbol{\Delta}_1^a \cdot \boldsymbol{\ell}_1 = R\chi_1\chi_3 \left\langle a|\mathcal{P}_h|\mathcal{V}\right\rangle, \quad [29]$$
$$\boldsymbol{\Delta}_2^a \cdot \boldsymbol{\ell}_2 = -R\chi_2\chi_4 \left\langle a|\mathcal{P}_v|\mathcal{V}\right\rangle, \quad [30]$$

where the bra $\langle a|$ projections the ket of vertex amplitudes, $|\mathcal{V}\rangle$ onto the amplitude of vertex a.

B. Lattice vector shears. Now, consider the shears of the lattice vectors computed by projection onto the transverse lattice vectors. While the projections no longer eliminate the face-dependent terms, $\mathbf{f}(A) \times \boldsymbol{\ell}$, compatibility of the linear isometries ensures that any path can be used to compute changes to the lattice vectors; in particular, the path can be constructed so that $\mathbf{f}_1(A) = \mathbf{f}_2(A) = \mathbf{f}(A)$ as illustrated by the solid gray path in Fig. S3A, thereby eliminating the face dependence since symmetrizing over the two lattice directions adds the terms as $\mathbf{f}(A)(\boldsymbol{\ell}_1 \times \boldsymbol{\ell}_2 + \boldsymbol{\ell}_2 \times \boldsymbol{\ell}_1)$. Careful choice of local basis for writing the lattice vectors shows that:

$$\boldsymbol{\Delta}_1^a \cdot \boldsymbol{\ell}_2 = \tau_1^A \hat{v}_1^a \times (-\mathbf{v}_3^a) \cdot (\mathbf{v}_2^a - \mathbf{v}_4^a) - \phi_2^{\mathcal{P}_h a} \hat{v}_2^{\mathcal{P}_h a} \times \mathbf{v}_1^{\mathcal{P}_h a} \cdot (\mathbf{v}_2^{\mathcal{P}_h a} - \mathbf{v}_4^{\mathcal{P}_h a}), \quad [31]$$
$$\boldsymbol{\Delta}_2^a \cdot \boldsymbol{\ell}_1 = \tau_4^A \hat{v}_2^a \times (-\mathbf{v}_4^a) \cdot (\mathbf{v}_1^a - \mathbf{v}_3^a) + \phi_1^{\mathcal{P}_v a} \hat{v}_1^{\mathcal{P}_v a} \times \mathbf{v}_2^{\mathcal{P}_v a} \cdot (\mathbf{v}_1^{\mathcal{P}_v a} - \mathbf{v}_3^{\mathcal{P}_v a}), \quad [32]$$

which simplifies by replacing the triple products with the associated vertex folding coefficients:

$$\boldsymbol{\Delta}_1^a \cdot \boldsymbol{\ell}_2 = \tau_1^A v_3^a \left(v_2^a \zeta_4^a + v_4^a \zeta_2^a\right) - \phi_2^{\mathcal{P}_h a} v_1^{\mathcal{P}_h a} v_4^{\mathcal{P}_h a} \zeta_3^{\mathcal{P}_h a}, \quad [33]$$
$$\boldsymbol{\Delta}_2^a \cdot \boldsymbol{\ell}_1 = \tau_4^A v_4^a \left(v_1^a \zeta_3^a + v_3^a \zeta_1^a\right) + \phi_1^{\mathcal{P}_v a} v_2^{\mathcal{P}_v a} v_3^{\mathcal{P}_v a} \zeta_4^{\mathcal{P}_h a}. \quad [34]$$

Finally, substitution of the local solutions yields:

$$\boldsymbol{\Delta}_1^a \cdot \boldsymbol{\ell}_2 = -\mathcal{F}^A v_1^a v_3^a \left(v_2^a \zeta_4^a + v_4^a \zeta_2^a\right) + \mathcal{V}^{\mathcal{P}_h a} v_3^a v_4^a \zeta_1^a \zeta_2^a, \quad [35]$$
$$\boldsymbol{\Delta}_2^a \cdot \boldsymbol{\ell}_1 = -\mathcal{F}^A v_2^a v_4^a \left(v_1^a \zeta_3^a + v_3^a \zeta_1^a\right) - \mathcal{V}^{\mathcal{P}_v a} v_3^a v_4^a \zeta_1^a \zeta_2^a, \quad [36]$$

and the symmetrized shear, $\boldsymbol{\Delta}_1 \cdot \boldsymbol{\ell}_2 + \boldsymbol{\Delta}_2 \cdot \boldsymbol{\ell}_1 = 0$, vanishes after invoking the relationship between the face and vertex amplitudes and averaging over all cells.

C. Lattice curvatures. Finally, consider the difference between two locally defined changes to the lattice vectors as indicated by the two distinct black paths shown in Fig. S3B. Since the linear isometries satisfy position closure, this difference is equal to a rotation of the edge between their vertices, $\mathbf{r}_{(a,a')}$, by the lattice angular velocity and a rotation of the lattice vector by the angular velocity gradient between their corners:

$$\mathbf{\Delta}_\mu^{(a',A')} - \mathbf{\Delta}_\mu^{(a,A)} = \mathbf{\Omega}_\mu \times \mathbf{r}_{(a,a')} + \left(\boldsymbol{\omega}^{(a,A)} - \boldsymbol{\omega}^{(a',A')}\right) \times \boldsymbol{\ell}_\mu. \quad [37]$$

Projecting this difference onto the same lattice vector eliminates the second term. Moreover, since the lattice angular velocity must lie in the plane spanned by the lattice vectors, the triple product simplifies $\mathbf{\Omega}_\mu \times \mathbf{r}_{(a,a')} \cdot \boldsymbol{\ell}_\mu = (\mathbf{r}_{(a,a')} \cdot \mathbf{N})(\mathbf{\Omega}_\mu \times \boldsymbol{\ell}_\mu \cdot \mathbf{N})$ Hence, the rotation of the lattice vector is characterized by the local dependence of the changes to the lattice vectors:

$$\kappa_{\mu\mu} \equiv \mathbf{\Omega}_\mu \times \boldsymbol{\ell}_\mu \cdot \mathbf{N} = -\frac{(\mathbf{\Delta}_\mu^{a'} - \mathbf{\Delta}_\mu^{a}) \cdot \boldsymbol{\ell}_\mu}{\mathbf{r}_{(a,a')} \cdot \mathbf{N}}, \quad [38]$$

where the corner dependence reduces to vertex dependence since the projection is onto the same lattice direction. This expression is valid for *any* two vertices in the unit cell.

The same analysis can be applied to transverse projections where the lattice vector rotations vanish after symmetrization:

$$\kappa_{\mu\nu} \equiv \mathbf{\Omega}_\mu \times \boldsymbol{\ell}_\nu \cdot \mathbf{N} = -\frac{(\mathbf{\Delta}_\mu^{a'} - \mathbf{\Delta}_\mu^{a}) \cdot \boldsymbol{\ell}_\nu + (\mathbf{\Delta}_\nu^{a'} - \mathbf{\Delta}_\nu^{a}) \cdot \boldsymbol{\ell}_\mu}{2\mathbf{r}_{(a,a')} \cdot \mathbf{N}}, \quad [39]$$

which satisfies equality because $\mathbf{\Omega}_\mu \times \boldsymbol{\ell}_\nu = \mathbf{\Omega}_\nu \times \boldsymbol{\ell}_\mu$ by compatibility. These off-diagonal curvatures are generated by the antisymmetric bend mode:

$$\kappa_{12}^{\text{asym}} = \frac{R}{4}\chi_{13}^{+}\chi_{24}^{+}, \quad [40]$$

as well as the twist mode:

$$\kappa_{12}^{\text{twist}} = -\frac{R}{2}. \quad [41]$$

D. Recovery of the Morph Poisson's ratio. The formalism presented in the main text enables a clear connection between the symmetry of generic four-parallelogram origami crease patterns and their equal-and-opposite in-plane and out-of-plane Poisson's ratios. Here, we show that our result recovers the prediction for the Morph subfamily derived via a more conventional formalism.

Consider the limit of the Morph subfamily of crease patterns where the in-plane response of our theory is experimentally validated in other work. This family is characterized by the edge lengths $c \equiv r_1 = r_3$, $a \equiv r_4$, and $b \equiv r_2 = a\cos\alpha/\cos\beta$ and the sector angles $\beta \equiv \alpha_A = \alpha_B$ and $\alpha \equiv \alpha_C = \alpha_D$. Our result for the in-plane Poisson's ratio is:

$$\nu_{\text{in}} = \frac{|\boldsymbol{\ell}_2|^2}{|\boldsymbol{\ell}_1|^2}\frac{\chi_2\chi_4}{\chi_1\chi_3} = \frac{|\boldsymbol{\ell}_2|^2}{|\boldsymbol{\ell}_1|^2}\frac{r_1 r_3}{r_2 r_4}\frac{\sin\gamma_1 \sin\gamma_3}{\sin\gamma_2\sin\gamma_4}, \quad [42]$$

(where the γ_i are dihedral angles) while the result for the Morph subfamily presented in Ref. (4) is:

$$\nu_{\text{in}} = \frac{|\boldsymbol{\ell}_2|^2}{|\boldsymbol{\ell}_1|^2}\frac{c^2\cos\beta}{a^2\cos\alpha}\frac{4\sin\alpha\sin\beta\cos\frac{\gamma_2}{2}\cos\frac{\gamma_4}{2}}{\sin^2\phi}, \quad [43]$$

,

where $\hat{r}_2 \cdot \hat{r}_4 = \cos\phi$. By assignment of the edge lengths, Eqn. (42) recovers Eqn. (43) provided that $\frac{4\sin\alpha\sin\beta\cos\frac{\gamma_2}{2}\cos\frac{\gamma_4}{2}}{\sin^2\phi} = \frac{\sin\gamma_1\sin\gamma_3}{\sin\gamma_2\sin\gamma_4}$. Application of the trigonometric law of sines shows that $\sin\phi = \sin\alpha\sin\gamma_1/\sin\frac{\gamma_2}{2} = \sin\beta\sin\gamma_1/\sin\frac{\gamma_4}{2}$, and the symmetry imposed by the sector angles of the Morph pattern implies that $\gamma_1 = \gamma_3$. Thus, invoking the trigonometric identity $\sin\frac{\gamma}{2}\cos\frac{\gamma}{2} = \frac{1}{2}\sin\gamma$ confirms that the two expressions are identical.

4. Lattice fundamental forms

In continuous two-dimensional sheets, strain and curvature correspond to changes in the diagonal components of the first and second fundamental forms respectively. Here, we discuss this connection and derive all of the components of analogous *lattice* fundamental forms for four-parallelogram origami.

A. Review of fundamental forms in continuous sheets. A continuous sheet is parameterized by coordinates on the two-dimensional surface which map to positions in the three-dimensional embedding space $\mathbf{X} = \mathbf{X}(x_1, x_2)$. The first fundamental form (metric tensor) of the sheet are the coefficients that measure arclengths on the sheet in terms of the surface coordinates. These coefficients are given by the tangent vectors, $\hat{t}_\mu \equiv \partial_\mu \mathbf{X}$, of the embedding:

$$I_{\mu\nu} = \hat{t}_\mu \cdot \hat{t}_\nu, \quad [44]$$

which is symmetric since the cross product is commutative. This first fundamental form becomes the identity, $I_{\mu\nu} = \delta_{\mu\nu}$, when the entire sheet lies in a plane and is diagonal when the tangent vectors are orthogonal, $\hat{t}_1 \cdot \hat{t}_2 = 0$. Infinitesimal changes to this quantity, $\delta\mathbf{I}$, give the strains of the sheet. The second fundamental form of the sheet are the coefficients that measure deflections of the sheet. These coefficients are given by the rotations of the tangent vectors, $\boldsymbol{\kappa}_{\mu\nu} \equiv \partial_\mu \hat{t}_\nu$, out of the plane:

$$II_{\mu\nu} = \boldsymbol{\kappa}_{\mu\nu} \cdot \mathbf{N}, \tag{45}$$

where $\mathbf{N} = \hat{t}_1 \times \hat{t}_2$ is the local normal vector of the sheet. The invariants of the second fundamental, $\mathbf{II}$, give the mean curvature, $H = \mathrm{Tr}\mathbf{II}$, and Gaussian curvature, $K = \mathrm{Det}\mathbf{II}/\mathrm{Det}\mathbf{I}$, which respectively vanish for flat and cylindrical (including flat) geometries. For initially flat sheets in particular, infinitesimal changes to the second fundamental form, $\delta\mathbf{II}$, are *exactly* the mean curvature, $H = \mathrm{Tr}\delta\mathbf{II}$, and the Gaussian curvature always vanishes to first-order in the deformation, $K = 0$.

B. Analogous fundamental forms in discretized sheets. A discretized origami sheet is instead parameterized by cell indices, $\mathbf{n} = (n_1, n_2)$, which map to positions in three-dimensional space via the lattice vectors, $\boldsymbol{\ell}_\mu$. Since the corrugation of the origami sheet suggests it functions closer to a slab than a membrane, it is appropriate to consider the geometry of the midplane defined as the average vertex position in each cell. The corresponding tangent vectors are the lattice vectors which do not rotate between cells so that the ground states have first and second lattice fundamental forms:

$$I_{\mu\nu} = \boldsymbol{\ell}_\mu \cdot \boldsymbol{\ell}_\nu, \tag{46}$$

$$II_{\mu\nu} = 0. \tag{47}$$

Recall that the lattice vectors are generically non-orthotropic, $\boldsymbol{\ell}_\mu \cdot \boldsymbol{\ell}_\nu \neq 0$, so that the off-diagonal components of the first lattice fundamental form in Eq. 46 are generically non-vanishing; however, since this dot product is an invariant as indicated in Eq. 2 it cannot change for rigid deformations which preserve the edge lengths and sector angles. Moreover, the first fundamental form can be diagonalized by performing a change of basis from the lattice vectors, $\boldsymbol{\ell}_\mu$, to a pair of orthogonal basis vectors, $\boldsymbol{\ell}'_\mu$. Without loss of generality let the first basis vector be identical to the first lattice vector, $\boldsymbol{\ell}'_1 \equiv \boldsymbol{\ell}_1$. The second basis vector is then obtained by Gram-Schmidt orthogonalization: $\boldsymbol{\ell}'_2 \equiv \boldsymbol{\ell}_2 - (\boldsymbol{\ell}_2 \cdot \hat{\boldsymbol{\ell}}'_1)\hat{\boldsymbol{\ell}}'_1$. The transformation between surface coordinates can then be obtained by application of the chain rule to the line elements

$$\Delta s^2 = I_{\mu\nu} \frac{\partial n_\mu}{\partial n'_\alpha} \frac{\partial n_\nu}{\partial n'_\beta} \Delta n'_\alpha \Delta n'_\beta = I'_{\alpha\beta} \Delta n'_\alpha \Delta n'_\beta, \tag{48}$$

and inverting the partial derivatives. This transformation can be applied to the strain and curvature of the lattice along orthogonal directions with the caveat that the Poisson's ratios are no longer equal and opposite.

C. Screw-periodic origami. More generic crease patterns have screw-periodic (cylindrical) ground states (7) for which the lattice vectors rotate between cells via the lattice rotations, $\mathbf{S}$, satisfying

$$\mathbf{S}_1\mathbf{S}_2 = \mathbf{S}_2\mathbf{S}_1, \tag{49}$$

$$\boldsymbol{\ell}_1 + \mathbf{S}_1\boldsymbol{\ell}_2 = \boldsymbol{\ell}_2 + \mathbf{S}_2\boldsymbol{\ell}_1. \tag{50}$$

The computation of the second lattice fundamental form would follow as:

$$II_{\mu\nu} = \mathbf{S}_\mu \boldsymbol{\ell}_\nu \cdot \mathbf{N}, \tag{51}$$

where $\mathbf{N} = \widehat{\boldsymbol{\ell}_1 \times \boldsymbol{\ell}_2}$ so that this quantity is automatically symmetric via Eq. (50). In this case, the zeroth-order second fundamental form *does not* correctly capture the curvature of the cylinder that this origami sheet discretizes; hence, this formalism must be augmented for more generic periodicities.

edge index	i	vertex amplitude	$\mathcal{V}$
vertex indices	a, b, c, d	face amplitude	$\mathcal{F}$
face indices	A, B, C, D	compatibility matrix	$\mathbf{C}$
global edge vector	$\mathbf{r}$	global folding coefficient	χ
local edge vector	$\mathbf{v}$	edge products	R
lattice vector	$\boldsymbol{\ell}$	change in lattice vector	$\boldsymbol{\Delta}$
permutation operator	$\mathcal{P}$	lattice angular velocity	$\boldsymbol{\Omega}$
angular velocity	$\boldsymbol{\omega}$	intercellular strain	ϵ
displacement	$\mathbf{u}$	intercellular curvature	κ
vertex folding angle	ϕ	Poisson's ratio	ν
local folding coefficient	ζ	sector angle	α
face bending angle	τ	dihedral angle	γ

Table S1. Notation used throughout the main text.

$\frac{\zeta_i}{v_i}$	a	b	c	d
1	χ_1	$-\chi_3$	χ_3	$-\chi_1$
2	χ_2	$-\chi_2$	χ_4	$-\chi_4$
3	$-\chi_3$	χ_1	$-\chi_1$	χ_3
4	$-\chi_4$	χ_4	$-\chi_2$	χ_2

Table S2. The local folding coefficients written in terms of the global folding coefficients.

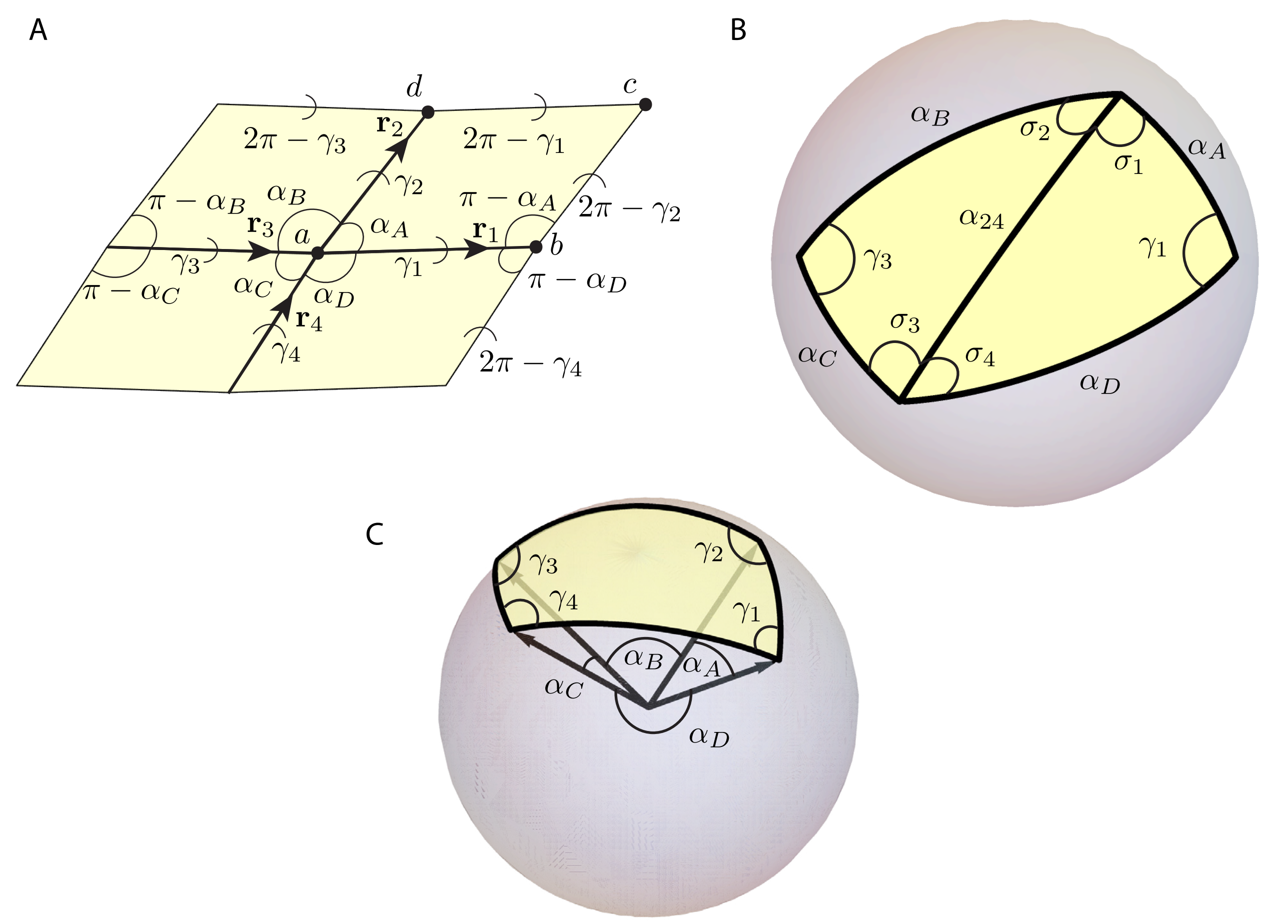

Fig. S1. (A) The unit cell of four-parallelogram origami is characterized by the four sector angles, α_A, α_B, α_C, and α_D which are identical at non-adjacent corners and supplementary, $\pi - \alpha$, in adjacent corners for parallelogram faces. The configuration of such a geometry is specified by the four dihedral angles, γ_1, γ_2, γ_3, and γ_4 which are complementary, $2\pi - \gamma$, on parallel edges to maintain spatial periodicity. (B) The projection of the central vertex in panel (A) onto the unit cell yields a spherical quadrilateral, whose edges have arc lengths subtending the sector angles and interior angles subtending the dihedral angles, that is triangulated via the great circle of arc length α_{24} which divides the interior angles $\gamma_2 = \sigma_1 + \sigma_2$ and $\gamma_4 = \sigma_3 + \sigma_4$. (C) Illustration of the projection of a four-coordinated vertex onto the unit sphere. The four arrows correspond to the directions of the edges emanating away from a vertex located at the center of the sphere.

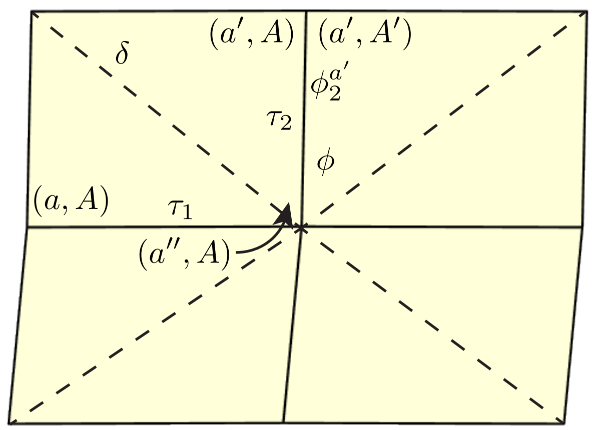

Fig. S2. Illustration of a triangulation of a four-parallelogram unit cell by the introduction of virtual creases (indicated by the dashed lines).

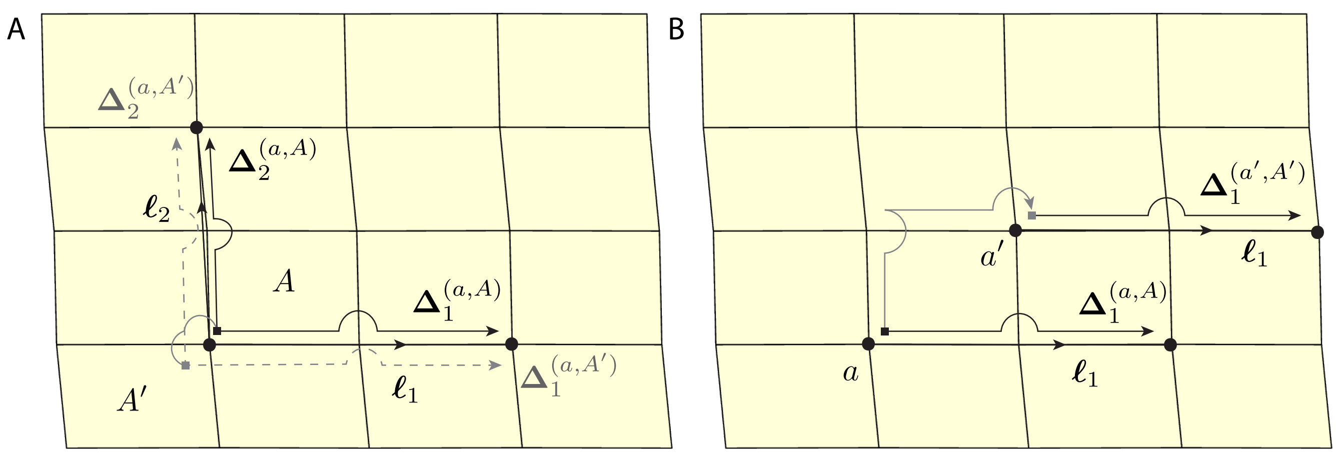

Fig. S3. An illustration of the local dependence on changes to the lattice vectors. (A) Changes to the lattice vectors depend on the face the corner is defined on as indicated by the dashed gray paths in contrast to the solid black paths. Linear compatibility allows these paths to be modified, as indicated by the solid gray path, thereby relating the changes in the lattice vector on all four corners in the vicinity of a single vertex. (B) Changes in the lattice vectors depend on the vertex the corner is defined on as indicated by the two black paths. Linear compatibility implies that this difference is given by the displacement computed along the solid gray path.

Movie S1. Animation of the rigid folding, along with the instantaneous Poisson's ratio and dihedral angles, of a four-parallelogram origami sheet with a connected configuration space.

Movie S2. Animation of the rigid folding, along with the instantaneous Poisson's ratio and dihedral angles, of a four-parallelogram origami sheet with a a disconnected configuration space.

Movie S3. Animation of the rigid folding, along with the instantaneous Poisson's ratio and dihedral angles, of a flat-foldable four-parallelogram origami sheet.

Movie S4. Animation of the rigid folding, along with the instantaneous Poisson's ratio and dihedral angles, of a generalized flat-foldable four-parallelogram origami sheet.

References

1. M Schenk, SD Guest, Geometry of miura-folded metamaterials. *Proc. Natl. Acad. Sci.* **110**, 3276–3281 (2013).
2. ZY Wei, ZV Guo, L Dudte, HY Liang, L Mahadevan, Geometric mechanics of periodic pleated origami. *Phys. review letters* **110**, 215501 (2013).
3. H Nassar, A Lebée, L Monasse, Curvature, metric and parametrization of origami tessellations: theory and application to the eggbox pattern. *Proc. Royal Soc. A: Math. Phys. Eng. Sci.* **473**, 20160705 (2017).
4. PP Pratapa, K Liu, GH Paulino, Geometric mechanics of origami patterns exhibiting poisson's ratio switch by breaking mountain and valley assignment. *Phys. review letters* **122**, 155501 (2019).
5. P Dieleman, N Vasmel, S Waitukaitis, M van Hecke, Jigsaw puzzle design of pluripotent origami. *Nat. Phys.* **16**, 63–68 (2020).
6. LH Dudte, GP Choi, L Mahadevan, An additive algorithm for origami design. *Proc. Natl. Acad. Sci.* **118** (2021).
7. J McInerney, BGg Chen, L Theran, CD Santangelo, DZ Rocklin, Hidden symmetries generate rigid folding mechanisms in periodic origami. *Proc. Natl. Acad. Sci.* **117**, 30252–30259 (2020).